This can be further improved by increasing the aspect ratio *W/L* of the antenna. However, as the aspect ratio decreases (for the 20 × 23 mm antenna), the two field components become comparable. For a 21 × 21 mm antenna with the proposed type of slot, we found that the antenna generates left-hand circular polarization [9]. The 3-dB axial-ratio bandwidth obtained was 2.8%. The impedance bandwidth is much wider. Note that if the slots are reversed, right-hand circular polarization results without any change to the antenna's impedance bandwidth.

REFERENCES

1. M. Ali, R.A. Sadler, and G.J. Hayes, A uniquely packaged internal inverted-F antenna for Bluetooth or wireless LAN application, IEEE Antennas Wireless Propagat Lett 1 (2002), 5–7.
2. K.V. Kumar, M. Ali, H.S. Hwang, and T. Sittironnarit, Study of a dual-band packaged patch antenna on a PC card for 5–6-GHz wireless LAN applications, Microwave Opt Technol Lett 37 (2003), 423–428.
3. M. Ali, T. Sittironnarit, H.-S. Hwang, R.A. Sadler, and G.J. Hayes, Wideband/dual-band packaged antenna for 5–6-GHz WLAN application, IEEE Trans Antennas Propagat (2004, to appear).
4. K.F. Tong, K.M. Luk, K.F. Lee, and R.Q. Lee, A broadband U-slot rectangular patch antenna on a microwave substrate, IEEE Trans Antennas Propagat 48 (2000), 954–960.
5. J.Y. Sze and K.L. Wong, Slotted rectangular microstrip antenna for bandwidth enhancement, IEEE Trans Antennas Propagat 48 (2000), 1149–1152.
6. C. Kidder, M. Ling, and K. Chang, Broadband U-slot patch antenna with a proximity coupled double Π-shaped feed line for arrays, IEEE Antennas Wireless Propagat Lett 1 (2002), 2–4.
7. F. Yang, X.X. Zhang, X. Ye, and Y. Rahmat-Samii, Wideband E-shaped patch antennas for wireless communications, IEEE Trans Antennas Propagat 49 (2001), 1094–1100.
8. Ansoft HFSS, Ansoft Corporation, http://www.ansoft.co.jp/hfss.htm.
9. M. Ali, R. Dougal, G. Yang, and H.-S. Hwang, Wideband (5–6-GHz WLAN band) circularly polarized patch antenna for wireless power sensors, IEEE Antennas Propagat Soc Int Symp Dig 2 (2003), 34–37.

FREQUENCY-SELECTIVE SURFACE BASED BANDPASS FILTERS IN THE NEAR-INFRARED REGION

Srikanth Govindaswamy,[1] Jack East,[1] Fred Terry,[1] Erdem Topsakal,[2] John L. Volakis,[3] and George I. Haddad[1]
[1] Solid State Electronics Laboratory
Electrical Engineering and Computer Science Department
University of Michigan
Ann Arbor, MI 48109
[2] Department of Electrical and Computer Engineering
Mississippi State University
Mississippi State, MS 39762
[3] Radiation Laboratory
Electrical Engineering and Computer Science Department
University of Michigan
Ann Arbor, MI 48109
He is also a Professor and the Director of ElectroScience Laboratory
Electrical Engineering Department
The Ohio State University
Columbus, OH 43212

ABSTRACT: *A spatial bandpass filter resonant at 1.5 μm and based on a frequency-selective surface (FSS) was analyzed and fabricated. It consists of circular apertures arranged in a hexagonal lattice and was modeled using a hybrid finite-element/boundary-integral method, which accounted for metal thickness and conductivity. Measurements demonstrate the accuracy of the design.* © 2004 Wiley Periodicals, Inc. Microwave Opt Technol Lett 41: 266–269, 2004; Published online in Wiley InterScience (www.interscience.wiley.com). DOI 10.1002/mop. 20112

1. INTRODUCTION

Frequency-selective surfaces (FSSs) consist of elements arranged in a planar periodic array to create a bandpass or bandstop filter. The properties of the filter can be varied by choosing the appropriate element type and its dimension and volumetric structure, and the spacing of the elements. The substrate also influences the behavior of the filter. FSSs have been used extensively in the microwave and millimeter region; hence, there is a good understanding of their behavior [1–3]. Of particular interest in this paper are FSSs operating in the near-infrared region. Analyses of FSSs at near-infrared frequencies were done in [4–9]. However, models of the metallization surface and the dielectric regions have been inadequate. Also, fabrication challenges exist because the critical dimensions of the FSS are less than 1 μm. In this paper, we consider a new model for the metallization region of the FSS, which is volumetric and recognizes the plasmalike behavior of the metal at infrared wavelengths. Measurements based on a newly fabricated FSS are also given to verify the proposed model and related analysis. Using electron-beam lithography, the FSS is constructed as an arrangement of circular holes designed to operate as a bandpass filter in the optical and near-infrared frequencies. In the following sections, we present the analysis and validation along with the results, which led to the fabrication choices. The fabrication process is also discussed.

2. BANDPASS FILTER MODELING

The bandpass filter was modeled using FSDA-PRISM, a code described in [11–13]. This code uses a hybrid finite element/boundary integral (FE/BI) to analyze the electromagnetic scattering and radiation characteristics of infinite periodic planar arrays and FSS configurations. The finite-element formulation is used within the volumetric region with the boundary integral employed to terminate the mesh. Prismatic elements are employed for volume discretization in the FE regions and triangular elements in the BI region. The FE region is used to model the inhomogeneous sections in the thick metal layers, whereas multilayered uniform sections are modeled using the multilayer Green's function [13], and the BI-computation is accelerated by using the fast spectral-domain algorithm (FSDA) [12]. The filter consists of circular apertures arranged in a hexagonal lattice. In the ideal case, the circles should have a diameter equal to about $\lambda/2$ and separated by λ, where λ is the desired resonant wavelength. However, the dimensions must be scaled if the filters are fabricated on top of a substrate.

The key to our modeling approach is the treatment of the metal layer (which incorporates the circular-aperture FSS) as a thick dielectric layer with appropriate dielectric constants and thicknesses [14]. The employed real and imaginary values of the electrical permittivity used in our model are given by

$$\varepsilon = \varepsilon_r + j\varepsilon_i = (n^2 - k^2) + j2nk,$$

where n and k are the real and imaginary values of the refractive index. These values are given in [15] for the wavelength range of
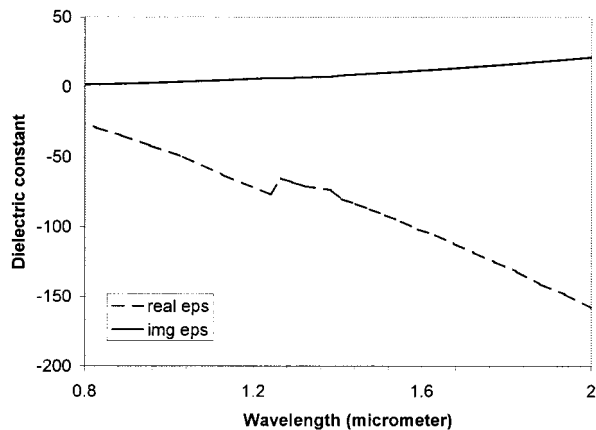
Figure 1 Calculated real and imaginary parts of the dielectric constant for gold [15]
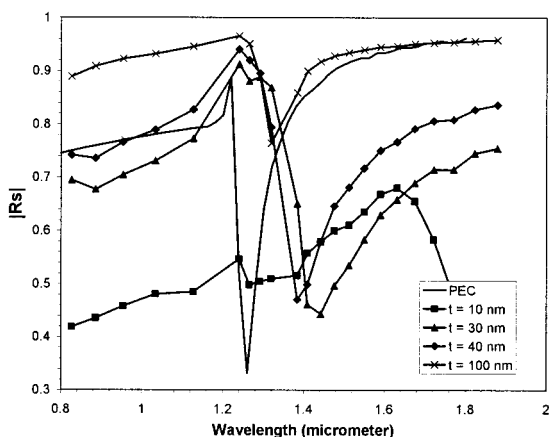

Figure 2 Simulated reflectance for the circular aperture FSS with a gold layer of finite thickness on a silicon substrate. The simulation based on a PEC FSS is also shown for comparison
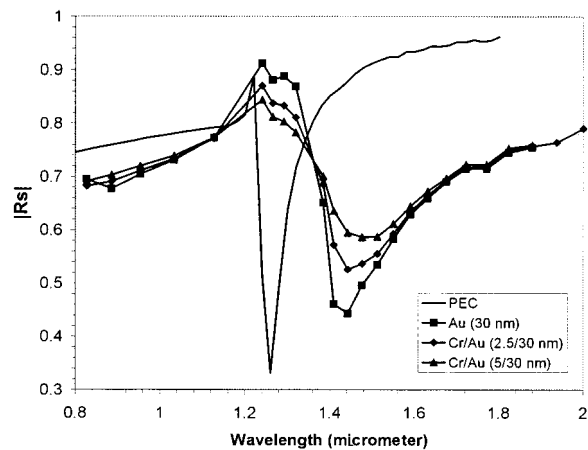

Figure 3 Simulated reflectance for the circular aperture FSS with different chromium-metal thicknesses between the gold and the silicon substrate (the gold layer is kept constant at 300 Å). The simulation based on a PEC FSS is also shown for comparison

0.8–2 μm (Fig. 1). The dielectric constants vary with frequency and affect the resonant wavelength and bandwidth of the filter.

For our study, let us consider a bandpass filter with a gold metal layer on a high-index silicon substrate ($\varepsilon_r = 11.7$). Gold has the lowest resistance among available metals and is therefore preferred. The FSS elements consist of circular apertures of 200-nm diameter and a center-to-center spacing of 400 nm. For this configuration, the reflectance for different gold-layer thicknesses is given in Figure 2. The ideal case in which the metal is replaced by a perfect electric conductor (PEC) is also shown for comparison.

The simulation, which is based on a PEC FSS, shows a resonance at ~1.25 μm with a reflection coefficient minimum of ~0.3. This value arises due to the difference between the refractive index of air and silicon. The onset of the grating lobe is observed at ~1.2 μm. In Figure 2, we also show the reflectance for different gold-layer thicknesses, ranging from 10 to 100 nm. We observe that when the thickness is 10 nm, the metal layer is semitransparent and no resonance is observed. The resonance becomes strong as the thickness increases to 30 nm. However, this occurs at a longer wavelength than the PEC case and the bandwidth is larger. This shift in the resonant wavelength and increase in bandwidth can be explained qualitatively using an equivalent RLC circuit [16]. The capacitance C and inductance L correspond to the apertures and the metal region, respectively. The resistance R refers to the ohmic

loss of the metal. The loss and increase in bandwidth is due to the finite conductivity of the metal, whereas the shift in resonance is due to the dielectric properties of the metal layers influencing the inductance and capacitance values. As the thickness of the metal layer increases beyond 40 nm, the apertures begin to act as a cylindrical waveguide. An additional insertion loss and reduction in bandwidth is also observed [17]. Eventually, a cutoff point would be reached where no propagation through the circular apertures is possible. For low insertion loss, we see an optimum range of 30–40 nm for the gold-metal thickness that can be used for the filter fabrication.

Gold alone adheres poorly to the silicon substrate. Chromium is therefore used as an adhesion promoter. Unfortunately, the addition of the chromium layer introduces more loss in the reflection spectrum. Chromium has nearly constant dielectric constant values in the wavelength range under consideration. For our simulation, we assumed a real and imaginary values of 1.76 and 38.7, respectively. The simulated reflectance R_s for TE excitation is plotted in Figure 3 for different chromium layers. The ideal case with a PEC is also plotted for comparison. The practical minimum chromium-layer thickness necessary (without severely compromising the coverage of the substrate surface) is about 25–30 Å. For a given gold layer of 30 nm, the minimum reflection values vary from 0.55 to 0.6 when chromium layers of 2.5 and 5 nm are used, respectively.

3. FILTER FABRICATION

An experimental version of the filter was fabricated on top of a silicon substrate using a two-stage process similar to that used by Byrne et al. [5]. A layer of oxide was deposited on top of the substrate using PECVD. Subsequently, a 100-nm layer of 950 K PMMA was spun on top of the oxide and patterned using a RAITH-150 electron-beam lithography system. The circular elements were defined as dots and exposed (defining the apertures as dots instead of circles helped reduce the exposure time). The accelerating voltage was 20 KV and the beam current was 24.8 pA. The exposed PMMA layer was developed in a 1:3 solution of methyl-isobutyl ketone (MIBK) and isopropyl alcohol (IPA) for 30 s and then immersed in a solution of isopropyl alcohol for 30 s. A layer of 50/450 Å Ti/Ni was then deposited and metal liftoff was performed. The metal layer was used as a mask layer to etch the
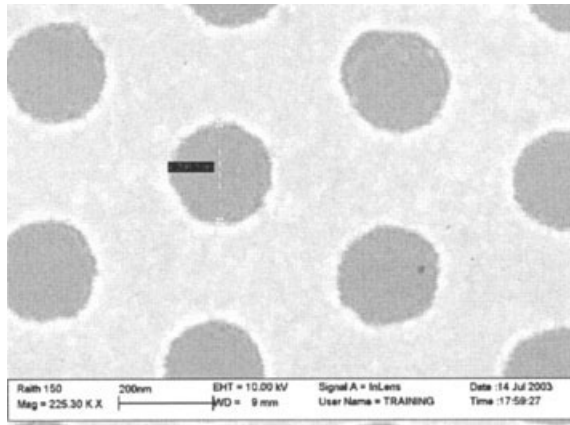
Figure 4 SEM photograph of the filter on top of a silicon substrate. Diameter of the circle is 200 nm with a spacing of 400 nm, and the metal thickness is 30/300 Å Cr/Au

oxide layer, thereby inverting the polarity of the exposed PMMA layer.

The parameters for etching the oxide layer were as follows: RF power = 180 W, CF_4 flow rate = 25 sccm, CHF_3 flow rate = 25 sccm, and pressure = 100 mTorr. The typical etch rate for the above parameters was 25 nm/minute. The oxide layer was over-etched to ensure that the oxide layer was removed from the exposed silicon layer. A second layer of 30/300 Å Cr/Au was then deposited. The metal on top of the oxide layer was removed by etching the sample in a BHF solution. Any remaining debris was removed using an adhesive tape. The fabricated filter using the above process is shown in Figure 4. The circular apertures had a diameter of ∼200 nm with a spacing of 400 nm.

4. MEASUREMENTS

The reflectance of the filter was measured using a SOPRA GESP-5 spectroscopic ellipsometry system. This system uses a photomultiplier for the 0.5–0.9-μm range and then switches over to an extended InGaAs photodetector for the 0.9–2-μm wavelength range. The plane wave was incident at 7° off-normal and the measurements were done for both TE (R_s) and TM (R_p) excitations. For calibration, we employed an aluminum coating on a silicon wafer. Our calibration was verified using a ∼2-μm SiO_2 layer (also on a silicon wafer).

Figure 5 shows the measured reflectance of the filter. The response for TE and TM excitations are identical, as expected for
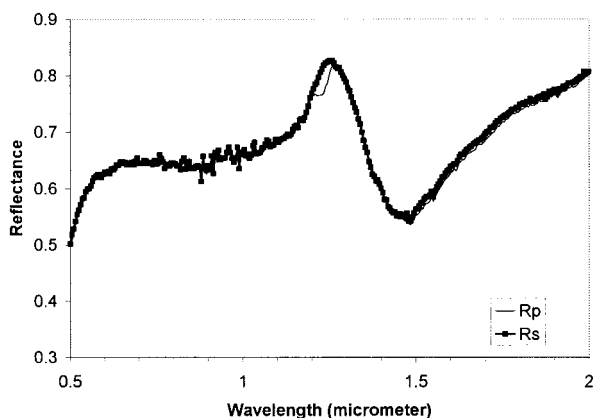

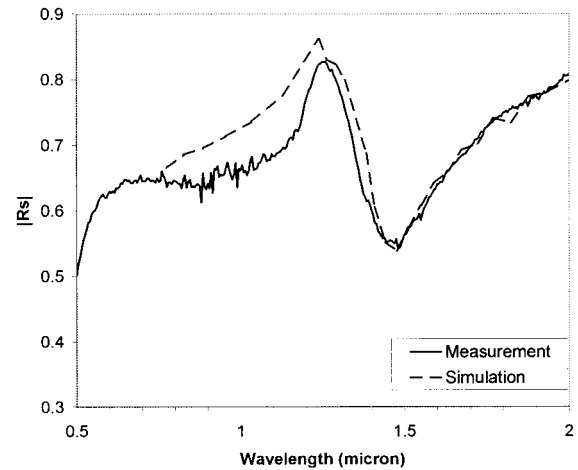**Figure 5** Measured spectral reflectance for TE/TM excitations

Figure 6 Simulated and measured spectral reflectance for TE excitation

a symmetrical element (in this case, circular aperture). The measured reflectance has a minimum value of ∼0.55 at 1.5 μm and, as expected, this value is limited by the loss in the metal layers and by the difference in the refractive index between the air and substrate. An antireflection coating would improve the performance of the filter. The onset of grating lobes was observed at ∼1.3 μm. For practical usage, this onset should be moved to smaller wavelengths. At this stage, our interest is to merely validate the model. Consequently, we did not pursue a modification of the design.

Figure 6 shows the simulated and measured reflectance of the filter for TE incidence, in which good agreement is observed. In particular, the resonant wavelength and the reflection minimum agree quite well.

5. CONCLUSIONS

A modeling approach for bandpass filters at near-infrared wavelength in which metal conductivity and thickness were accounted for using a complex permittivity valid at the subject wavelengths has been presented. We found that there is an optimum range for metal thicknesses that can be used in the fabrication of such filters. Below this range, the metal is semitransparent and resonance is poor. For thicker metals, the aperture can act like a waveguide and cutoff is observed. Filters were fabricated and characterized to demonstrate the accuracy of our new volumetric model for metals, which acts like a plasma at near-infrared regions.

REFERENCES

1. J.C. Vardaxoglou, Frequency-selective surfaces: Analysis and design, Research Studies Press, Ltd., Taunton, UK, 1997.
2. T.K. Wu, Frequency-selective surface and grid array, Wiley, New York, 1995.
3. B.A. Munk, Frequency-selective surfaces: Theory and design, Wiley, New York, 2000.
4. C.M. Rhoads, E.K. Damon, and B.A. Munk, Mid-infrared filters using conducting elements, Appl Optics 21 (1982), 2814–2816.
5. D.M. Byrne, A.J. Brouns, F.C. Case, R.C. Tiberio, B.L. Whitehead, and E.D. Wolf, Infrared mesh filters fabricated by electron-beam lithography, J Vac Sci Technol 3 (1985), 268–271.
6. I. Puscasu, W.L. Schaich, and G.D. Boreman, Modeling parameters for

the spectral behavior of infrared frequency-selective surfaces, Appl Optics 40 (2001), 118–124.

7. S.J. Spectro, D.K. Astolfi, S.P. Doran, T.M. Lyszczarz, and J.E. Raynolds, Infrared frequency-selective surfaces fabricated using optical lithography and phase-shift masks, J Vac Sci Technol B 9 (2001), 2757–2760.

8. K.E. Paul, C. Zhu, J.C. Love, and G.M. Whitesides, Fabrication of mid-infrared frequency selective surfaces by soft lithography, Appl Optics 40 (2001), 4557–4561.

9. M.D. Morgan, W.E. Horne, V. Sundaram, J.C. Wolfe, S.V. Pendharkar, and R. Tiberio, Fabrication of optical filters fabricated by masked ion beam lithography, J Vac Sci Technol B 14 (1996), 3903–3906.

10. M. Bozzi and L. Perregrini, Efficient analysis of FSS with arbitrarily shaped patches by the MoM/BI-RME method, IEEE Antennas Propagat Soc Int Symp Dig 4 (2001), 390–393.

11. T.F. Eibert, J.L. Volakis, D.R. Wilton, and D.R. Jackson, Hybrid FE/BI modeling of 3D doubly periodic structures utilizing triangular prismatic elements and an MPIE formulation accelerated by the Ewald transformation, IEEE Trans Antennas Propag 47 (1999), 843–850.

12. T.F. Eibert and J.L. Volakis, Fast spectral domain algorithm for hybrid finite element/boundary integral modeling of doubly periodic structures, IEE Proc Microwave Antennas Propagat 147 (2000), 329–334.

13. T.F. Eibert, Y.E. Erdemli, and J.L. Volakis, Hybrid finite-element fast spectral domain multilayer boundary integral modeling of doubly periodic structures, IEEE Trans Antennas Propagat 51 (2003), 2517–2520.

14. E. Topsakal and J. Volakis, On the properties of materials for designing filters at optical frequencies, IEEE Antennas Propagat Soc Int Symp 4 (2003), 635–638.

15. E.D. Palik, Handbook of optical constants of solids, Academic Press, Orlando, FL, 1985.

16. J.E. Reynolds, B.A. Munk, J.B. Pryor, and R.J. Marhefka, Ohmic loss in frequency selective surface, J Appl Phys 93 (2003), 5346–5358.

17. R.J. Luebbers and B.A. Munk, Analysis of thick rectangular waveguide windows with finite conductivity, IEEE Trans Microwave Theory Tech 21 (1973), 461–468.

BROADBAND PRINTED π-SHAPED MONOPOLE ANTENNA FOR WLAN OPERATION

Saou-Wen Su,[1] Chih-Hsien Wu,[1] Wen-Shyang Chen,[2] and Kin-Lu Wong[1]
[1] Department of Electrical Engineering
National Sun Yat-Sen University
Kaohsiung 804, Taiwan
[2] Department of Electronic Engineering
Cheng Shiu University
Kaohsiung 833, Taiwan

ABSTRACT: *A broadband printed π-shaped monopole antenna is presented. The antenna is easily achieved by adding two short vertical strips (one is a feeding strip and one is a short-circuiting strip) to a long horizontal strip, forming into a π shape with a low profile. This antenna can generate a wide bandwidth (about 29%) formed by two separate, but closely spaced, resonant modes. A prototype well suited for covering the 5.2/5.8-GHz WLAN bands and operating as an internal antenna for a wireless device is demonstrated.* © 2004 Wiley Periodicals, Inc. Microwave Opt Technol Lett 41: 269–270, 2004; Published online in Wiley InterScience (www.interscience.wiley.com). DOI 10.1002/mop.20113
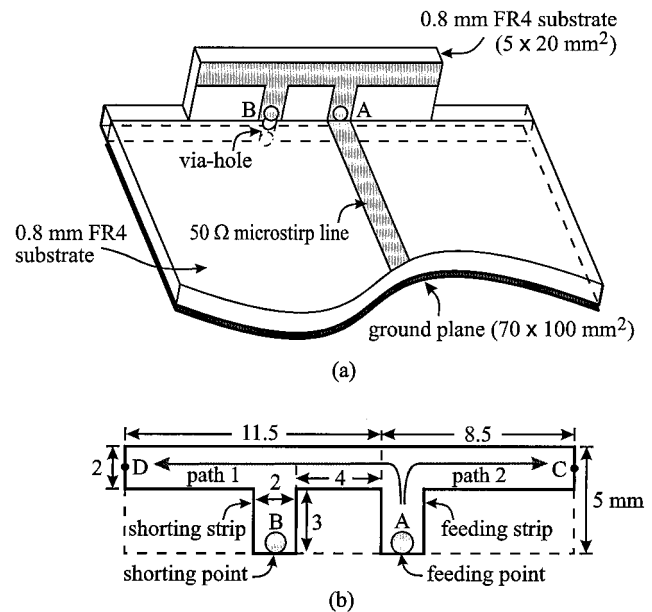
Figure 1 (a) Geometry of the proposed π-shaped monopole antenna mounted at the top edge of a grounded substrate; (b) dimensions of the π-shaped monopole

1. INTRODUCTION

Monopole antennas with low profile and wide bandwidth are attractive and frequently in demand for applications in handheld devices for wireless communications [1]. In this paper, we propose a novel broadband π-shaped monopole antenna to meet this demand. The proposed antenna can be treated as two inverted-L monopoles [2] of different sizes arranged back to back, with the larger inverted-L monopole short-circuited to the ground plane. The two different inverted-L monopoles generate two separate, but closely spaced, resonant modes, which are then formed into a wide operating band. The short-circuiting introduces additional inductance to compensate for the large capacitance generated between the monopole's horizontal strip and the ground plane; hence, good impedance matching for frequencies across the two closely excited resonant modes becomes easy to achieve. A design example of the proposed antenna for operating in the 5.2/5.8-GHz (5150–5350/5725–5875 MHz) bands for wireless local-area network (WLAN) operation is presented.

2. ANTENNA DESIGN

Figure 1(a) shows the geometry of the proposed π-shaped monopole antenna mounted at the top edge of a grounded substrate, which has a size of approximately 70×100 mm², which is about the size of the system circuit board of a practical personal digital assistant (PDA) device. Figure 1(b) shows the dimensions of the π-shaped monopole printed on a 0.8-mm supporting substrate (of size 5×20 mm²), which is mounted vertically to the system ground plane. With the proposed arrangement, the π-shaped monopole has a very small protruded length (0.8 mm) from the top edge of the ground plane, such that it can easily be embedded within the casing of a PDA device for WLAN operation; that is, an internal WLAN antenna can be achieved.

As shown in Figure 1(b), the π-shaped monopole comprises a long horizontal strip of length 20 mm and two short vertical strips of length 3 mm, with all the strip widths set to 2 mm. One vertical strip is connected to a 50Ω microstrip feedline at point A (feeding point), and the second one is short-circuited to the ground plane